The variable iron K emission line in MCG−6-30-15

K. Iwasawa,[1] A. C. Fabian,[1] C. S. Reynolds,[1] K. Nandra,[2] C. Otani,[3] H. Inoue,[4]
K. Hayashida,[5] W. N. Brandt,[1] T. Dotani,[4] H. Kunieda,[6] M. Matsuoka[3] and Y. Tanaka[4,7]

[1]*Institute of Astronomy, Madingley Road, Cambridge CB3 0HA*
[2]*Laboratory for High Energy Astrophysics, Goddard Space Flight Center, Greenbelt, MD 20771, USA*
[3]*The Institute of Physical and Chemical Research (RIKEN), Hirosawa, Wako, Saitama 351-01, Japan*
[4]*Institute of the Space and Astronautical Science, Yoshino-dai, Sagamihara, Kanagawa 229, Japan*
[5]*Department of Earth and Space Science, Osaka University, Toyonaka, Osaka 560, Japan*
[6]*Department of Astrophysics, Nagoya University, Chikusa-ku, Nagoya 464-01, Japan*
[7]*Max-Plank Institut für Extraterrestrische Physik, Giessenbachstrasse, D-85740 Garching, Germany*

ABSTRACT
We report on the variability of the iron K emission line in the Seyfert 1 galaxy MCG−6-30-15
during a four-day *ASCA* observation. The line consists of a narrow core at an energy of about
6.4 keV, and a broad red wing extending to below 5 keV, which are interpreted as line emission
arising from the inner parts of an accretion disc. The narrow core correlates well with the
continuum flux whereas the broad wing weakly anticorrelates. When the source is brightest,
the line is dominated by the narrow core, whilst, during a deep minimum, the narrow core is
very weak and a huge red tail appears. However, at other times when the continuum shows
rather rapid changes, the broad wing is more variable than the narrow core, and shows
evidence for correlated changes contrary to its long-time-scale behaviour. The peculiar line
profile during the deep minimum spectrum suggests that the line-emitting region is very close
to a central spinning (Kerr) black hole where enormous gravitational effects operate.

Key words: accretion, accretion discs – line: profiles – galaxies: individual: MCG−6-30-15
– X-rays: galaxies.

1 INTRODUCTION

ASCA observations have revealed that iron K emission lines in the
X-ray spectra of many Seyfert 1 galaxies are broad (Kunieda 1995;
Mushotzky et al. 1995; Tanaka et al. 1995; Iwasawa et al. 1996;
Yaqoob et al. 1995; Fabian et al. 1995 and references therein). The
presence of a fluorescent iron Kα line and a high-energy hump
above 10 keV in the *Ginga* spectra (e.g. Pounds et al. 1990; Nandra
& Pounds 1994) has been explained by reflection from cold thick
material subtending a large solid angle (~2π sr) at the X-ray source.
An accretion disc can realize such a geometry and velocities
implied from the resolved linewidths, which greatly exceed those
in the optical broad-line region, support it.

A recent long (~4.5 d) *ASCA* observation of the bright Seyfert 1
galaxy MCG−6-30-15 has provided the best-resolved line profile so
far (Tanaka et al. 1995). The iron Kα emission line is broad and
skewed to low energies, with little emission above the rest energy of
6.4 keV, close to the line peak, and considerable emission down to 5
keV. The immediate interpretation of the line is that it originates by
fluorescence in the very inner part of an accretion disc (e.g. within
$20r_g$) about a massive black hole, illuminated by a primary X-ray
source. The line shape and skewness are due to the combined effects
of Doppler shifts and gravitational redshift from matter in a deep
gravitational potential well, moving in directions within 30° from

perpendicular to the line of sight. Since no other plausible broad-
ening mechanism appears to work (Fabian et al. 1995), we will
discuss the line properties in the framework of the 'disc-line'
model.

MCG−6-30-15 is a nearby Seyfert 1 galaxy ($z = 0.008$), and one
of the best-studied active galaxies in X-ray wavebands (Nandra,
Pounds & Stewart 1990; Nandra & Pounds 1994; Fabian et al. 1994;
Reynolds et al. 1995). This galaxy usually shows large-amplitude
X-ray flux changes on time-scales of hours and days. This makes it a
good target for studying the response of the line to continuum
changes. However, the line flux is too low to study short time-scales
and we can only sensibly comment on changes, or lack of changes,
on time-scales of longer than 10^4 s. The count rate attributable to the
line is ~5×10^{-3} count s^{-1}, meaning that each detector accumulates
about 100 count per line component per 4×10^4 s which is a large
fraction of an operational day. In a simple illumination model we
could expect the line to follow the continuum, with lags for the light
crossing time (see e.g. Stella 1990). Since this time is much shorter
than a day (it is $500r_1M_7$ s at $10r_1$ gravitational radii for a black hole
of mass $10^7 M_7$ M$_\odot$), we do not expect to detect any lag. As we shall
demonstrate, changes are still observed, the explanation for which
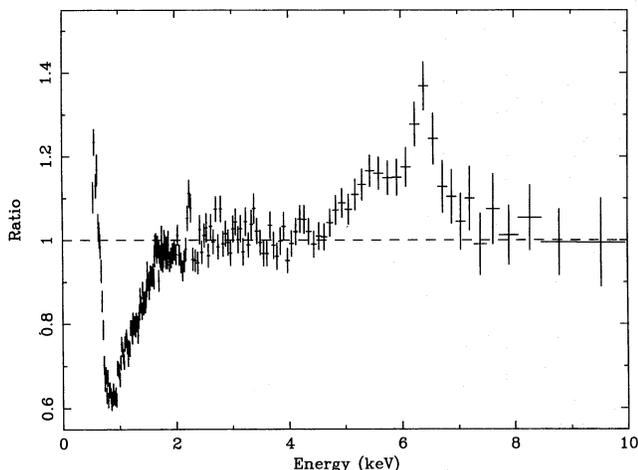is less straightforward.

We detect significant line profile changes during the observation
in which the continuum varies with a maximum amplitude of a

factor of 7. The importance of transverse Doppler and gravitational redshift increases as the region where the line originates comes closer to the central hole. If the line arises from an accretion disc about a black hole, the line shape (Fabian et al. 1989; Laor 1991) and its variations therefore provide information about the location and movement of the line-emitting regions. The changes imply that the spatial distribution of the emission is not constant with time. This is the first step in mapping the inner accretion flow of an active galactic nucleus.
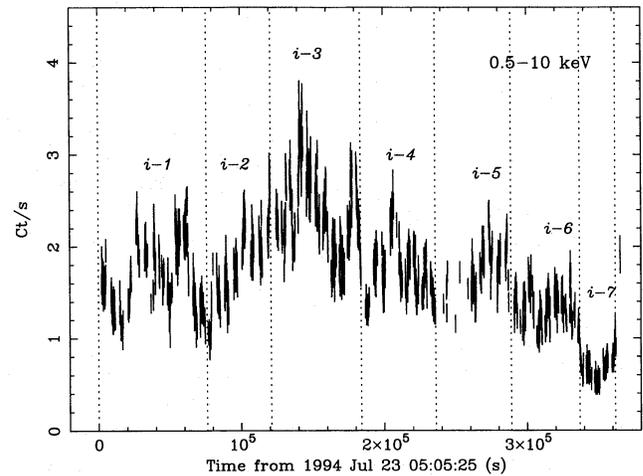
2 OBSERVATIONS AND DATA REDUCTION

MCG−6-30-15 was observed by *ASCA* (Tanaka, Inoue & Holt 1994) from 1994 July 23 to 27, with the Solid-state Imaging Spectrometer (SIS) in Faint/1CCD mode and the Gas Imaging Spectrometer (GIS) in pulse height (PH) mode. The most well-calibrated chip was chosen for the observation in each SIS. Data reduction was performed using the *ASCA* standard software, FTOOLS and XSELECT.

The presence of a spectral feature owing to partially ionized gas in the line of sight, the so-called 'warm absorber', established in this source (Nandra & Pounds 1992; Fabian et al. 1994; Reynolds et al. 1995), has been studied in detail for the same observation (Otani et al. 1996). The spectral distortion of the incident power law owing to this is known to affect changes below 2 keV (Fig. 1; also e.g. Fabian et al. 1994). To avoid this complexity, we use the 3−10 keV data for spectral analysis. A detailed description of the SIS data selection is given by Otani et al. (1996). The data taken when the source elevation is between 5° and 25° above the bright Earth are also used here, although contrary to standard practice, since our restriction to hard X-ray data renders these data usable. About 200 ks of data are left for spectral analysis, and the X-ray light curve from a single SIS detector (S0) in the 0.5−10 keV band is given in Fig. 2. For GIS spectra, we applied the standard data selection criteria: source elevation higher than 5° above the Earth rim, cut-off rigidity larger than 6 GeV c^{-1}, and the spacecraft not in the South Atlantic

Figure 2. The 0.5−10 keV light curve from the S0. The epoch of the start of the light curve is 1994 July 23 05:05:25. Each data bin is averaged over 128 s. The seven time intervals used in the Section 3.2 are indicated in the figure (see Table 1).

Anomaly (SAA). The GIS is relatively insensitive to the line shape, because it has worse spectral resolution than the SIS. On the other hand, the GIS has better efficiency over the higher energy band above 5 keV. Owing to these complementary characteristics of the two detectors, we mainly use the SIS data to characterize the line shape, and the GIS data to help determine continuum slopes. The background data are taken from a nearby blank field in the same detector field of view for each data set with the same time coverage.

3 RESULTS

3.1 Spectral fitting

The underlying continuum is fitted by a single power law absorbed by the Galactic column density ($N_H \approx 4 \times 10^{20}$ cm^{-2}). Even though a strong high-energy hump in the *Ginga* spectrum above 10 keV is known in this source (e.g. Nandra & Pounds 1994), this reflection component affects the line flux by only ~5 per cent in observed *ASCA* spectra. In the following study, spectra from shorter intervals have fewer counts than in the total spectrum so the statistical error dominates the uncertainties on the line intensity.

Modelling of the characteristic shape of the line is basically carried out in two ways: a double-Gaussian or a disc-line model. In fits with two Gaussians, we assume line energies and dispersions for the narrow and broad components to be the same as for the total spectrum (Tanaka et al. 1995), unless noted otherwise: $E_B = 5.5$ keV, $\sigma_B = 0.64$ keV for the broad component, and $E_N = 6.40$ keV, $\sigma_N = 0.15$ keV for the narrow component. The line flux of each component is derived from the SIS spectra, because the separation of the two components is not appropriate for the GIS energy resolution.

The disc-line model for a Schwarzschild geometry by Fabian et al. (1989) is used in most cases, assuming a cold accretion disc inclined at 30° (Tanaka et al. 1995). Among the parameters of the disc-line, the rest line energy, $E = 6.4$ keV appropriate for K-shell emission from iron less ionized than Fe XVII, and disc inclination, $i = 30°$, are used. The other parameters are the radial emissivity index, α, assuming a power-law-type radial emissivity function ($\propto R^{-\alpha}$) of the line, inner radius, R_{in}, of the disc of which the innermost radius of stable orbit for Schwarzschild geometry is $6r_g$,

Figure 1. The ratio of data and model for the averaged 0.4−10 keV spectrum of MCG−6-30-15. The data are obtained from the S0 detector integrating over the entire long observation (exposure time ~1.7 × 10^5 s). The model is a single power law of photon index $\Gamma = 1.96$ modified by cold absorption, $N_H = 6 \times 10^{20}$ cm^{-2}, fitted to the data excluding the 0.7−2.5 keV and the 4.5−7.2 keV bands. There is a clear absorption feature around 1 keV, mainly due to O VII and O VIII in the warm absorber, and a broad iron K emission line around 6 keV. Note that the effect of the warm absorber is restricted to below 2 keV.

Table 1. The seven data sets. Count rates in the 3–10 keV band from S0 and S1 are given. The time range for each data set is shown in Fig. 2.

Data	Exposure 10^3 s	3–10 keV count s^{-1}	Time range 10^4 s
i-1	43.4	0.274/0.218	0.0–7.6
i-2	22.2	0.273/0.212	7.6–12.1
i-3	36.1	0.390/0.301	12.1–18.2
i-4	27.2	0.296/0.235	18.2–23.5
i-5	26.1	0.295/0.239	23.5–28.8
i-6	30.4	0.243/0.185	28.8–33.7
i-7	15.2	0.152/0.120	33.7–36.2

disc outer radius, $R_{\rm out}$, and normalization of the line. The inner and outer radii are in units of gravitational radius, $r_{\rm g} = GM/c^2$. Errors quoted to best-fitting values are at the 90 per cent confidence level for one interesting parameter, while data points in plots have 1σ error bars.

3.2 Spectra selected in time sequence

We now investigate spectral changes in time sequence. The X-ray source shows a large flare in the middle of the observation, and a deep minimum of about 25-ks duration near the end. Including the two extremes, the whole observing run was divided into seven time intervals with a similar exposure time (~ 30 ks) as shown in Table 1 and Fig. 2. The pairs *i-1* and *i-2*, and *i-4* and *i-5* have similar continuum fluxes to each other.

We present evidence of a spectral change between the 'bright flare' (*i-3*) and the 'deep minimum' (*i-7*) in Fig. 3, which is obtained by taking the ratio of *i-7* minus *i-3* to a power-law model. The photon index of the power law ($\Gamma = 2.0 \pm 0.3$) is obtained by fitting the data in which the iron line band (4–7 keV) is excluded, and is consistent with the average continuum slope. If the line flux
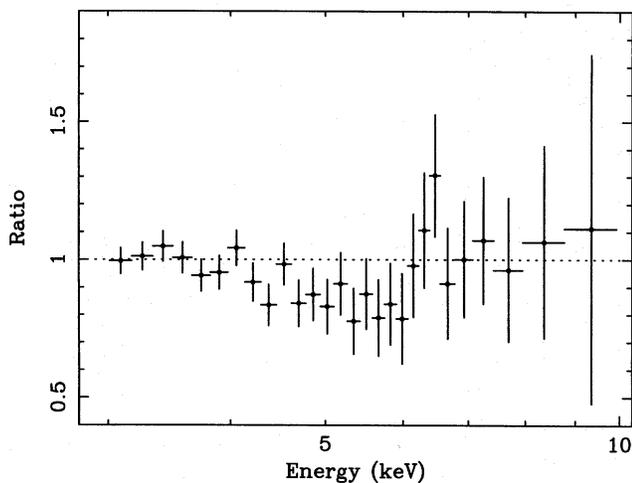
Figure 3. The ratio of 'bright flare minus deep minimum' data to a power law with a photon index of $\Gamma = 2.0$. The power law is fitted to the data excluding the iron K line band (4–7 keV). This plot demonstrates changes in spectral shape taking place between the two extreme flux levels. A deficit from 4 keV to 6.4 keV can be seen with a clear peak at 6.4 keV. This implies an intensity decrease in the broad wing band and an increase in the narrow core band.

followed the continuum and there were no change in line profile or continuum shape taking place between the two intervals, the subtracted spectrum would show a line profile similar to the time-averaged line shape as shown in Fig. 1. A narrow peak at 6.4 keV is therefore understood as resulting from an increase of the narrow core following the continuum change. A clear broad deficit around 5 keV, however, suggests a decrease of the broad red wing, contrary to expectation. An alternative explanation for the broad deficit could be a complicated spectral change in continuum from effects of the warm absorber and reflection. This possibility will be investigated in detail for the deep minimum data, where also a clear change in the warm absorber is found (Otani et al. 1996).

3.2.1 Double-Gaussian fits

The results of the double-Gaussian fit to the seven data sets are given in Table 2. Owing to the greater efficiency above 5 keV of the GIS, the continuum slopes are best determined by the GIS spectra. Therefore, in fitting the SIS data, the photon index is constrained to range within the 90 per cent confidence limits obtained from the GIS result. The photon indices are very similar from *i-1* to *i-5* at around $\Gamma \approx 1.98$. A flatter continuum is suggested for *i-6* and *i-7* where the continuum flux is low. A slope change there is, however, statistically insignificant. The line energy of the narrow component fluctuates slightly around the rest energy of 6.4 keV from data set to data set, if allowed to be a free parameter (e.g. 6.55 ± 0.15 keV in *i-5*), but it is always consistent with 6.4 keV; the precise value does not significantly affect the line intensities obtained.

Fig. 4 shows the behaviour of the broad and narrow components as a function of the continuum flux. The intensities of the two components show the opposite behaviour. The narrow component is correlated well with the continuum flux. On the other hand, the broad component shows a weak anticorrelation. As a result, the narrow core is more variable than the broad wing, although varying in the opposite manner.

The ratios of the broad and narrow components in the bright flare and the deep minimum data are clearly different from those of the other five data sets at intermediate flux levels (Fig. 5). This indicates that the line profile has changed significantly at least in the two time intervals *i-3* and *i-7*. The equivalent width of the narrow component is statistically constant through all the data sets. If the narrow component maintains a constant equivalent width (EW), then the changes of line profile are due to the broad red wing since the EWs of the broad component in *i-3* and *i-7* are significantly different from the rest.

To clarify the changes in intensity of the narrow and broad components and the ratio of the two, we also show a contour plot of the broad component versus the narrow component for the bright flare (*i-3*), the deep minimum (*i-7*), and a summed data set of *i-1*, *i-2*, *i-4* and *i-5*, obtained from the double-Gaussian fits (Fig. 6). The four data sets for the summed intermediate data have similar continuum flux levels and spectral shape as seen in Figs 4 and 5; the *i-6* data set is dropped here because of its slightly flatter spectral slope.

We present the line profiles obtained from the bright flare, the deep minimum, and the summed data set from the intermediate flux level (Fig. 7). The three line profiles have been fitted by the disc-line model, details of which are given below.
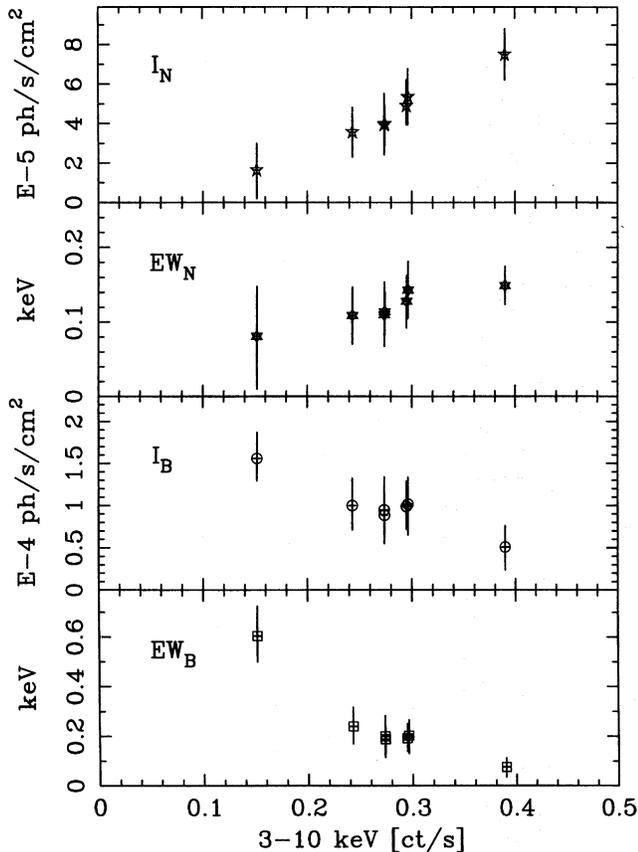
3.2.2 Intermediate flux data (*i-1, i-2, i-4* and *i-5*)

When the continuum flux is at an intermediate level, the line shape shows both a narrow core and a broad red wing, similar to

Table 2. Double-Gaussian fits to the seven data sets. The S0 and S1 data are fitted jointly. The best-fitting photon indices Γ for the SIS spectra are given with the 90 per cent confidence range obtained from the GIS spectra, in parentheses. Γ is allowed to vary within the GIS range (see text). Line energy and dispersion for each Gaussian are $E_N = 6.40$ keV and $\sigma_N = 0.15$ keV for the narrow component, and $E_B = 5.5$ keV and $\sigma_B = 0.64$ keV for the broad component through all the fits. Note that equivalent widths of the broad component are calculated at the centroid energy of 5.5 keV.

Data	Γ		I_N 10^{-5}ph s^{-1} cm^{-2}	EW_N eV	I_B 10^{-4}ph s^{-1} cm^{-2}	EW_B eV	χ^2/dof
i-1	2.00	(1.96–2.05)	$4.00^{+1.59}_{-1.63}$	114^{+45}_{-46}	$0.88^{+0.31}_{-0.31}$	189^{+68}_{-67}	398.8/471
i-2	1.92	(1.82–1.99)	$3.95^{+1.82}_{-1.89}$	110^{+52}_{-54}	$0.95^{+0.36}_{-0.49}$	200^{+78}_{-106}	381.7/415
i-3	2.02	(1.91–2.02)	$7.50^{+2.07}_{-2.10}$	149^{+42}_{-43}	$0.51^{+0.40}_{-0.48}$	76^{+61}_{-72}	489.6/499
i-4	2.01	(1.94–2.07)	$5.36^{+2.28}_{-2.38}$	143^{+61}_{-64}	$1.02^{+0.58}_{-0.61}$	203^{+117}_{-123}	349.3/415
i-5	1.97	(1.97–2.08)	$4.91^{+2.74}_{-1.90}$	128^{+75}_{-52}	$0.99^{+0.44}_{-0.42}$	193^{+87}_{-83}	324.9/409
i-6	1.86	(1.81–1.94)	$3.58^{+2.05}_{-1.94}$	109^{+64}_{-61}	$0.99^{+0.51}_{-0.49}$	240^{+123}_{-118}	357.0/394
i-7	1.75	(1.67–1.96)	$1.64^{+2.24}_{-1.64}$	81^{+112}_{-81}	$1.56^{+0.40}_{-0.56}$	605^{+145}_{-203}	158.1/171

the time-averaged line in Tanaka et al. (1995). The double-Gaussian fit to the line profile integrated over *i-1*, *i-2*, *i-4* and *i-5* gives the contour of narrow versus broad component intensities in Fig. 6 and the narrow/broad component ratio of 0.33 ± 0.10.

The line is well fitted by the disc-line model with $\alpha = 3.0 \pm 1.0$, $R_{in} = (7.6 \pm 1.4)r_g$, $R_{out} = 31^{+30}_{-8} r_g$, and a line flux of $1.35^{+0.28}_{-0.23} \times 10^{-4}$ photon s^{-1} cm^{-2} ($\chi^2 = 597.4$ for 642 degrees of freedom). The equivalent width of the line is EW $= 402^{+83}_{-68}$ eV. A combination of relatively large R_{out} and steep α obtained here could describe the averaged profile over the four intervals.

3.2.3 The bright flare phase (i-3)

The line shape in this spectrum raises difficulties in the disc-line fit, owing to a strong narrow core. As the double-Gaussian fit shows, the broad red wing is relatively fainter than in other intervals and its EW of 76 eV is significantly smaller than the others.

The narrow-line shape can be fitted by a disc-line model with a very large R_{out} (e.g. ~1000 r_g when $\alpha = 1$), which is indistinguishable from a single Gaussian in the present data. The quality of the fit is worse than the double-Gaussian model by $\Delta\chi^2 \approx 4$. However, problems in this model are not only that the red wing is no longer present in the profile and that the big jump in R_{out} by a factor of 50 or more is unlikely, but also that the continuum becomes only a few times brighter. Even if we take an extremely flat or even negative emissivity index (e.g. $\alpha = -3$), it does not work.
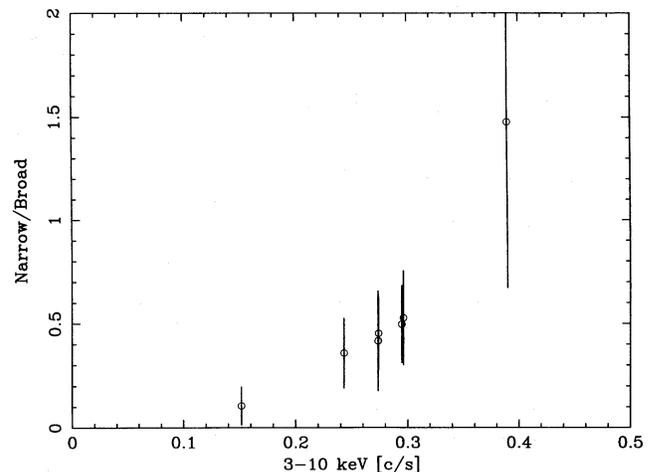

Figure 4. Plot of intensities and equivalent widths of the narrow and broad components as a function of the 3–10 keV count rate (from S0). The narrow component correlates positively with the continuum flux whereas the broad component is a decreasing function of continuum. The correlation coefficient is 0.983 for the narrow component intensity (I_N) and 0.960 for the broad one (I_B), implying statistical significances above 99.9 per cent for both. A constant equivalent width for the narrow component cannot be ruled out on statistical grounds.

Figure 5. Ratio of the narrow and broad components as a function of the 3–10 keV count rate. Intensities of both components are from the double-Gaussian fits in Fig. 4.
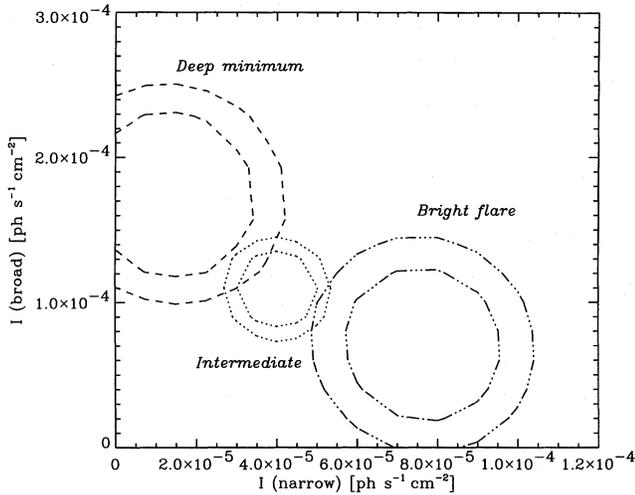
Figure 6. Contours of the broad versus narrow component intensities for the bright flare (*i-3*: dash-dotted line), intermediate fluxes (*i-1, i-2, i-4* and *i-5*: dotted line), and deep minimum (*i-7*: dashed line). Contour levels are at 68 and 90 per cent. Line profiles of the three data sets are shown in Fig. 7.
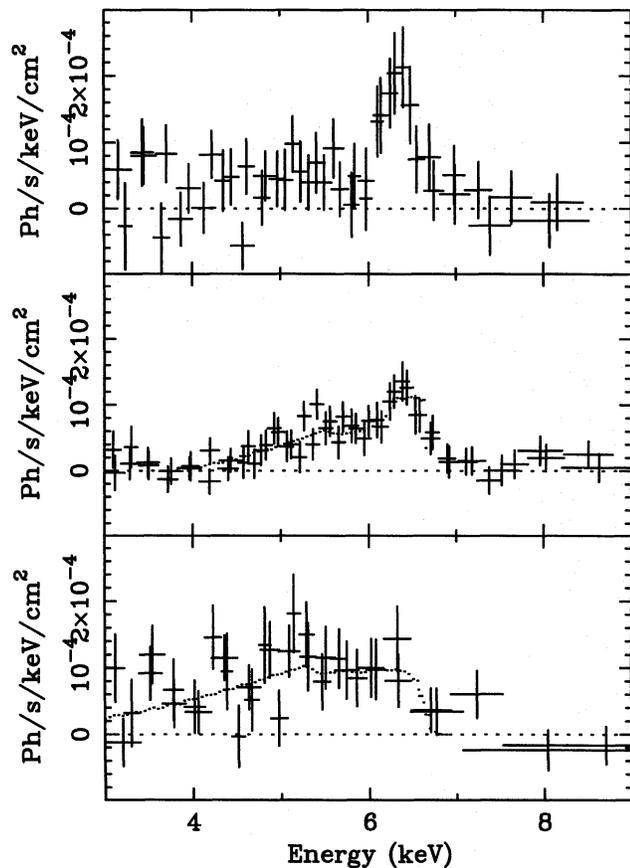
Figure 7. Line profiles corrected for detector response for interval 3 (the bright flare: upper panel), *i-1, i-2, i-4* and *i-5* summed (intermediate flux intervals: middle panel), and interval 7 (the deep minimum: lower panel). The line shape changes between the three flux levels are clearly seen. The best-fitting disc-line models for the intermediate flux data and the deep minimum data are indicated with dotted lines. The model for the deep minimum is L91 with a line energy of 6.4 keV as listed in Table 3.

We therefore introduce a phenomenological model of the disc-line plus an additional Gaussian to fit the line profile. This model, in which the disc-line has the parameters of the 'intermediate flux' data set, improves the quality of fit. The fraction of the extra narrow component modelled by a Gaussian is now about one-half the total line flux.

Since the EW of the narrow component implied from the double-Gaussian fit is not significantly different from that in the other intervals (Table 2 and Fig. 4), the peculiar line profile characterized by a large narrow-core/red-wing ratio (Fig. 5) is probably due to the suppression of the red wing. This may imply that the inner radii are less important for line production, or that the line emission from the red (receding) side of the disc is missing.

3.2.4   The deep minimum phase (i-7)

In contrast to the flare spectrum, the *i-7* spectrum shows the opposite appearance. Modelling with a double Gaussian shows no significant detection of the narrow-line component around 6.4 keV (see Table 2 and Fig. 4), but within the uncertainties its EW can remain constant at about 120 eV. The hypothesis of no emission line is, however, unlikely. A single-power-law fit leaves a large negative discrepancy in the data above 7 keV, relative to the model spectrum. If we introduce a sharp or a smeared edge, such as is seen in the spectra of Galactic black hole candidates (Ebisawa 1991), the fit requires an unreasonably flat spectral slope ($\Gamma \sim 1.2$), and an extremely deep edge (optical depth $\tau \sim 1$) at 7 keV. Extrapolation of such a continuum to the low-energy band below 3 keV is also incompatible with the data. This model is therefore ruled out, and we conclude that there is a strong broad component.

Since a huge red wing may be primarily produced in the innermost parts of the disc, we set the minimum value for the inner radius as $R_{in} = 6r_g$, the last stable orbit in the Schwarzschild geometry. The best-fitting emissivity index is then $\alpha = 3.2 \pm 3$, but the quality of the fit is significantly worse than that of the double-Gaussian fit ($\Delta\chi^2 \approx -6$), mainly owing to the fact that the model cannot explain the large red wing. A solution for this problem is obtained by introducing the Kerr geometry of a spinning black hole, which allows a smaller radius for the last stable orbit ($1.24r_g$), following the line profiles calculated by Laor (1991). This model provides an improved fit with a very similar χ^2 value to that for the double-Gaussian fit (Table 3). In this fit, the radial emissivity index is considerably well constrained ($\alpha = 2.7^{+0.7}_{-1.2}$). The line intensity is found to be even larger than the total value for the double-Gaussian fit by ~40 per cent.

As noted before (for Fig. 3), a strong red wing could, however, be due to complicated continuum effects from the warm absorber and reflection rather than the change in the line, since we have modelled the continuum by a simple power law modified by only Galactic absorption while the warm absorber increased over this interval (Otani et al. 1996). We examine such a possibility here by fitting the spectrum of the whole energy range (0.4–10 keV) with a model including the warm absorber and reflection continuum. To avoid possible contamination of the low-energy data by reflection from the sunlit Earth, data taken when the source is at an elevation angle below 25° from the bright Earth rim are discarded. The absorption column density of cold matter is fixed at the Galactic value ($N_H = 4 \times 10^{20}$ cm^{-2}).

The warm absorber in MCG–6-30-15 is usually described with two edges due to O VII at 0.73 keV and O VIII at 0.92 keV (Fabian et al. 1994; Reynolds et al. 1995; Otani et al. 1996). Even though the O VIII absorber is pronounced in this interval, the edge model for

Table 3. Disc-line fit to the *i-7* spectum. 'F89' is for a Schwarzschild geometry calculated by Fabian et al. (1989) whilst 'L91' is for a Kerr geometry by Laor (1991). R_{in} and R_{out} are set to the minimum value for each geometry ($6r_g$ for Schwarzschild geometry, and $1.25r_g$ for Kerr geometry), and $15.5r_g$, respectively. The disc inclination is assumed to be 30°. Γ is a free parameter within the range given in Table 2.

Model	E keV	α	R_{in} r_g	R_{out} r_g	I_{line} $10^{-4} \mathrm{ph\,s^{-1}\,cm^{-2}}$	EW eV	Γ	χ^2/dof
F89	6.4	3.2 ± 3	6	15.5	$1.69^{+0.51}_{-0.49}$	796^{+240}_{-231}	1.75	164.2/171
L91	6.4	$2.7^{+0.8}_{-1.2}$	1.24	15.5	$2.57^{+1.03}_{-0.87}$	1260^{+505}_{-427}	1.75	159.5/171
L91	6.7	$3.4^{+0.6}_{-0.8}$	1.24	15.5	$3.44^{+1.21}_{-1.07}$	1370^{+480}_{-430}	1.78	158.0/171

O VIII alone does not reach up to 3 keV, and absorption by the other elements is needed if the continuum above 3 keV is to be modified. We therefore model a multi-element warm absorber using a photo-ionization model computed with the CLOUDY code (Ferland 1991). This gives a good fit to the present data with a column density $N_W \approx 1.6 \times 10^{22}$ cm^{-2} and ionization parameter $\xi \approx 49$–53. The warm absorber with these parameters reduces the flux of a power-law continuum of $\Gamma = 1.9$ by about 10 per cent at 3 keV. A power law modified by the warm absorber alone does not describe the data well because it leaves a broad bump around 5 keV (Model 1 in Table 4).

Next we investigate the effect of adding an additional reflection component. The Compton reflection spectrum from cold matter computed in the form of Lightman & White (1988) is used here. We continue to assume that the inclination of the reflecting matter is 30°, and keep the solid angle of the subtending reflecting matter at the X-ray source, in units of 2π sr (i.e. solid angle of the reflecting material $\Omega/2\pi$), as a free parameter. As mentioned before, the reflection spectrum where $\Omega/2\pi = 1$, expected from normal reflection from an accretion disc, has little effect on the broad line. To assess whether pronounced reflection can explain the broad feature, this parameter is allowed to be above the physically reasonable value, i.e. $\Omega/2\pi > 2$.

We first fit the 0.4–10 keV spectrum of *i-7* by this warm absorber plus reflection model with no iron K emission line (Model 2 in

Table 4). Fitting the S0 and S1 detectors jointly gives $\Gamma = 1.92^{+0.2}_{-0.5}$ and $\Omega/2\pi = 12 \pm 4$ with $\chi^2 = 509.2$ for 444 degrees of freedom. Despite the fit giving an extremely large value for $\Omega/2\pi$, there is still a broad-line-like residual. This is because the broad feature is too sharp to be explained by the reflection spectrum. Also data above 7 keV are far below the model, implying that the predicted reflection hump is too strong. We therefore conclude that the warm absorber and pronounced reflection cannot explain the broad-line feature totally, even if unusually strong reflection is considered. In fact, significantly better fits are obtained by adding a double-Gaussian model or a disc-line model for a Kerr black hole (Models 3 and 4 in Table 4). Results of these fits are summarized in Table 4.

The best-fitting line intensities are consistent with those obtained from the previous fits to the 3–10 keV data. In the fits including the disc-line model for the broad iron line, constraints on the strength of reflection are poor and no strong reflection is necessary for a good fit to the data. The equivalent width of the line from the disc-line (L91 in Table 4) against the power-law plus reflection continuum is still large (EW = $1.28^{+0.53}_{-0.43}$ keV). The data of *i-7* in the 0.4–10 keV band and the best-fitting model including the warm absorber, reflection and the disc-line are shown in Fig. 8.

In summary, the warm absorber and the reflection slightly modify the 3–10 keV continuum, but do not affect the broad-line

Table 4. Fits to the 0.4–10 keV spectrum of *i-7* including the warm absorber and reflection. Models 1 and 2 do not have any iron line component. The warm absorber is computed using CLOUDY (Ferland 1991); parameters are the equivalent hydrogen column density (N_W) and ionization parameter ($\xi = L/nR^2$) of the ionized material. The reflection spectrum from a cold slab inclined by 30° is computed following Lightman & White (1988), allowing $\Omega/2\pi$ to vary. The disc-line model of Laor (1991) for Kerr geometry is fitted here using the rest line energy of 6.4 keV and the same inner and outer radii of the disc as those in Table 3. The radial line emissivity index (α) and normalization (I) are free parameters.

Model	Γ	Warm absorber $\log N_W$ cm^{-2}	ξ erg cm s^{-1}	Reflection $\Omega/2\pi$	Fe K line		χ^2/dof
1	$1.79^{+0.02}_{-0.03}$	22.43	78.96	—	—		534.6/445
2	$1.91^{+0.03}_{-0.04}$	22.16	51.05	12^{+4}_{-4}	—		509.2/444
					Double-Gaussian		
					I_N $\mathrm{ph\,s^{-1}\,cm^{-2}}$	I_B $\mathrm{ph\,s^{-1}\,cm^{-2}}$	
3	$1.89^{+0.03}_{-0.05}$	22.18	52.72	$2.4^{+4.0}_{-2.4}$	$2.50^{+2.88}_{-2.42} \times 10^{-5}$	$1.83^{+0.66}_{-0.49} \times 10^{-4}$	484.9/442
					Discline (L91)		
					α	I $\mathrm{ph\,s^{-1}\,cm^{-2}}$	
4	$1.92^{+0.05}_{-0.04}$	22.14	49.04	$3.7^{+4.2}_{-3.3}$	$2.6^{+0.9}_{-1.3}$	$2.72^{+1.14}_{-0.92} \times 10^{-4}$	482.3/442
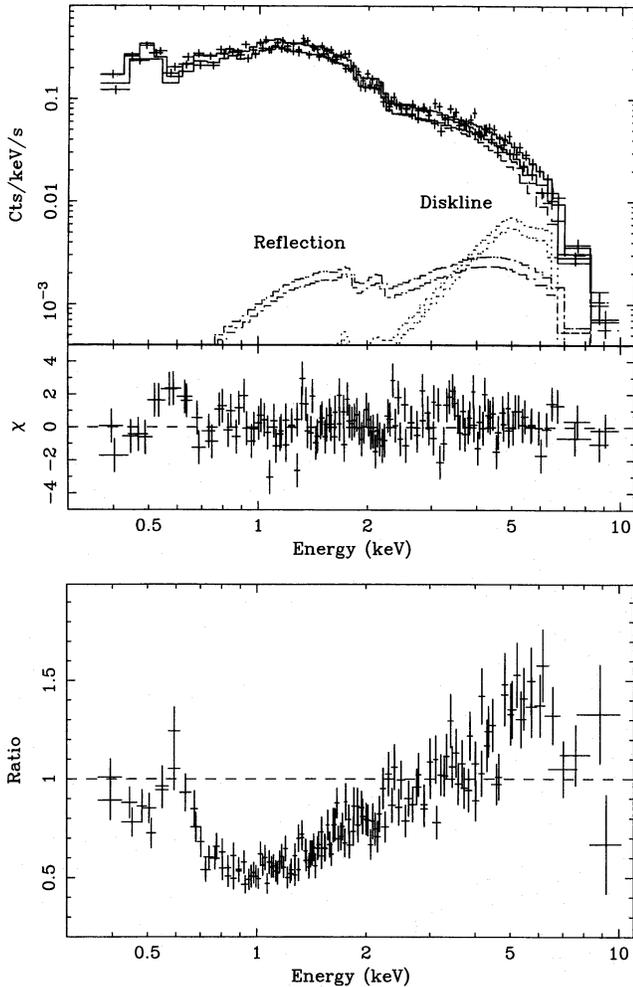
Figure 8. Upper panel: the 0.4–10 keV SIS spectrum of MCG–6–30–15 during the deep minimum (*i-7*). The data are fitted by a power law modified by the warm absorber computed by CLOUDY (Ferland 1991), a reflection spectrum from cold material (Lightman & White 1988), and a disc-line model for a Kerr metric from Laor (1991). The best-fitting-parameters are shown in Table 4 and the model spectrum folded through the X-ray telescope and the detector response of *ASCA* is displayed in the figure. The residuals at 0.6 keV are most likely an instrumental artefact. Lower panel: ratio of the data and continuum (power-law plus reflection). The plot is produced by setting the normalizations of the line and column density of the warm absorber to zero after making the best fit with the above model.

result seriously. Thus the strong broad red wing of the line in the *i-7* spectrum appears to be real from the above arguments, and the broad deficit seen in Fig. 3 is due not to continuum effects but to a change in the broad line. The line profile dominated by a broad red wing may be produced in regions very close to a central hole where the line is modified seriously by the gravitational redshift. The unusually large equivalent width may then be a problem. However, enhancement of reflection owing to the radiation returning to the disc (Cunningham 1976) may be relevant here (see Section 4).

3.3   Intensity-sorted spectra

We have found significant changes in both intensity and line profile when the data are sorted in time sequence. They are evident in the bright flare and the deep minimum data sets but not in the other

intervals, mainly because of similar averaged continuum levels. That study followed the behaviour of the line averaged over each selected time interval of a few $\times 10^4$ s. However, the continuum changes on shorter time-scales ($< 10^4$ s). If the line follows the continuum with a very short time lag, intensity-sorted spectra should show the response on short time-scales of the line.

We first investigate spectra obtained by intensity-sorting the whole data set (Section 3.3.1). However, dramatic changes in the line associated with large continuum variations on longer time-scales, such as for *i-3* and *i-7*, confuse the result. Excluding the bright flare and the deep minimum, changes in the X-ray source are in the intermediate range ($\sim 1-3$ count s^{-1} in the 0.5–10 keV band in Fig. 2) and on short time-scales of less than 10^4 s. To clarify the response of the line as close as possible to faster continuum changes in the intermediate flux range, we now examine the intensity-sorted spectra, excluding the two time intervals showing the longer time-scale changes (Section 3.3.2). All spectral fits are performed using the double-Gaussian model.

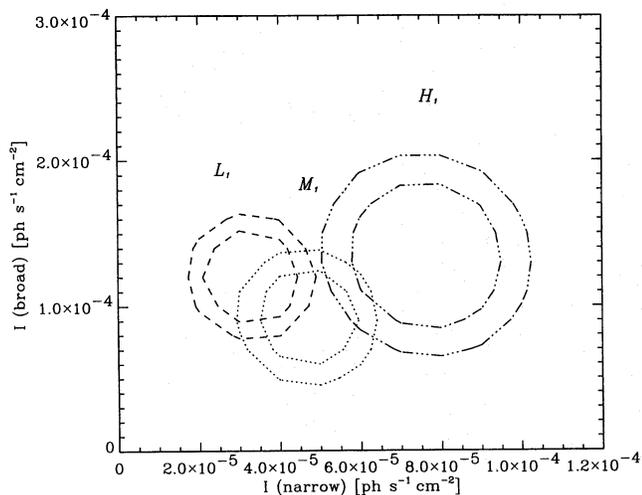### 3.3.1   The whole data set

We decompose the whole data set into three flux ranges as shown in Table 5: L_1 (low), M_1 (medium), and H_1 (high), using the count rate in the 0.5–10 keV light curve averaged over each 128 s. This decomposition was made using the S0 light curve (Fig. 2), and data from S1 are extracted from the same time region.

Fits with the double-Gaussian model show the line variation of the continuum intensity-sorted data. Contours of the broad versus narrow component intensities for the three flux levels are shown in Fig. 9. The narrow component increases as the continuum increases in a roughly proportional manner, whereas the broad component is not a simple increasing function of the continuum as the L_1 data show too strong a broad component. From Fig. 9, the ratio of the broad and narrow components is consistent between the H_1 and the M_1 data, indicating that the line profiles are similar there. However, the contour of the L_1 data is marginally above the region consistent with a constant narrow/broad component ratio. In these fits, the continuum photon index is constant within the 90 per cent errors: $\Gamma = 1.99 \pm 0.05$ in the H_1 and M_1 spectra and a slightly flatter $\Gamma = 1.92 \pm 0.06$ in the L_1 data.

This result shows that the narrow component has a positive correlation with the continuum, but the broad component may not, at least when the flux drops, as the L_1 data show a marginally stronger broad component than expected from the correlation. The narrow-line behaviour is consistent with the time-ordered data sets

Table 5. Intensity-sorted data sets of H_1 (high), M_1 (medium) and L_1 (low) intensity ranges for the whole SIS data set. Data are sorted according to the count rate in the 0.5–10 keV S0 light curve. Selected ranges of count rate are given in the second column. Averaged count rates from each S0 and S1 detector in the 3–10 keV band over the integration time are indicated.

Data	Range count s^{-1}	3–10 keV count s^{-1}	Exposure 10^3 s
H_1	> 2.2	0.413/0.318	45.2
M_1	1.6–2.2	0.320/0.253	72.6
L_1	< 1.6	0.223/0.178	74.2

Figure 9. Contours of intensities between the broad- and narrow-line components for the intensity-decomposed data from the whole data set. The contours are plotted as dash-dotted lines for the H_1, dotted lines for the M_1, and dashed lines for the L_1 data. The contour levels are at 68 and 90 per cent for the two interesting parameters.

Figure 10. Contours of intensities in the broad versus narrow components for intensity-sorted data sets (H_2: dash-dotted line; M_2: dotted line; and L_2: dashed line) excluding the time intervals of the bright flare and the deep minimum. Contour levels are at 68 and 90 per cent for the two interesting parameters.

shown in the previous section, although a significant correlation between the broad component and the continuum is not seen. This difference may be due to effects from the different data sorting methods. It will become clearer in the next study where we restrict data to the intermediate flux range.
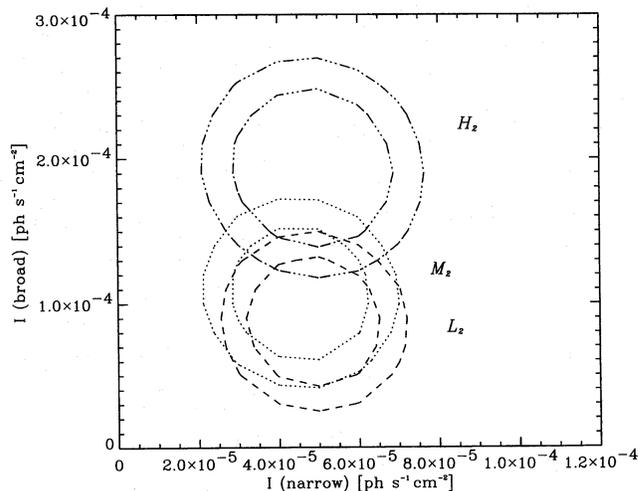
3.3.2 Intermediate flux range data

Using intensity-sorted spectra, we exclude two time regions of $1.3 \times 10^5 - 1.7 \times 10^5$ s (a major flare in *i-3*) and $3.4 \times 10^5 - 3.7 \times 10^5$ s. The selected count rate ranges, averaged count rates and integration times of three spectra are summarized in Table 6. We fit the double-Gaussian model and show a contour plot between the broad- and narrow-line intensities for each spectrum in Fig 10. Surprisingly the narrow component is consistent with a constant intensity, in contrast to the correlated behaviour with the continuum in time-ordered data sets (Section 3.2; see also Fig. 4). A significant line flux increase is found in the broad component of the high-flux data (H_2), and the result in Fig. 10 is consistent with the broad component correlating with the continuum flux. These are opposite behaviours to the results from data sets sorted in time order.

The selection for the high-flux data (H_2) here mainly picked up

many brief flares, and the result suggests that the broad component of the line follows the continuum rapidly, in 10^4 s or less. The increase of the broad component accompanying the brief flares is opposite to the decrease during the bright flare. This suggests that a different process is dominating line production in flares of longer and shorter time-scales.

3.4 A count rate ratio study of rapid variability

Finally, light curves of selected energy bands for the broad red wing (B; 4.6–6.2 keV), the narrow core (N; 6.2–6.7 keV) and the neighbouring continuum (C; 2.4–4.6 keV) are studied with data binned every 4048 s. From these light curves, we made ratio plots: (1) the narrow core band to the continuum band (N/C); (2) the red wing band to the continuum band (B/C); and (3) the narrow core band to the red wing band (N/B), averaging the S0 and S1 detectors.
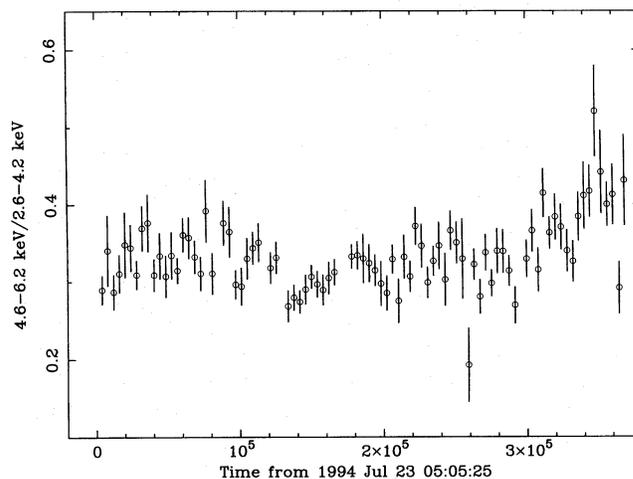
Figure 11. Time variation of the count rate ratio of the broad red wing band (4.6–6.2 keV) and the neighbouring continuum band (2.6–4.2 keV) from averaged data from S0 and S1. Each data point is integrated over 4048 s (some data points have an integration time of less than 4048 s).

Table 6. Intensity-sorted data sets excluding the bright flare and the deep minimum. Data are sorted according to the count rate in the 0.5–10 keV S0 light curve. Selected ranges of count rate are given in the second column. Averaged count rates from each S0 and S1 detector in the 3–10 keV band over the integration time are indicated.

Data	Range count s^{-1}	3–10 keV count s^{-1}	Exposure 10^3 s
H_2	> 1.9	0.372/0.300	38.4
M_2	1.6–1.9	0.304/0.240	41.1
L_2	< 1.6	0.251/0.192	42.0

The hypothesis that the data are constant was assessed by the chi-squared test. Chi-squared values for the best-fitting constant model are 77.52 for $N/C = 0.048 \pm 0.02$, 182.9 for $B/C = 0.321 \pm 0.04$, and 71.87 for $N/B = 0.146 \pm 0.04$, for 84 degrees of freedom.

Significant variation is found only in the B/C light curve (Fig. 11). Increases of B/C in the last part of the observation are partly due to the warm absorber (10–20 per cent; 0.03–0.07 in the B/C). Nevertheless there is also a decrease during the bright flare. The lack of any significant result from N/B is mostly due to poor statistics.

4   DISCUSSION

### 4.1   The black hole and accretion disc in MCG–6-30-15

MCG–6-30-15 continues to show significant continuum variability (i.e. factor of ~ 2 changes) over a wide range of time-scales from about 100 s (Reynolds et al. 1995) to days. If we assume that the iron line is at 6.4 keV and thus that the disc is not ionized, then the accretion must be at most a few per cent of the Eddington rate (Ross & Fabian 1993). The observed X-ray luminosity (0.5–10 keV) is ~10^{43} erg s^{-1} so it is likely that the mass of the black hole, in terms of $10^7 M_7 M_\odot$, is $M_7 \gtrsim 1$. For a typical emission radius of $10 r_1 r_g$, with $r_1 \approx 1$, the light-crossing time (of that radius) is then $500 M_7 r_1$ s and the orbital period is $10^4 M_7 r_1^{3/2}$ s. Unless M_7 is 0.2 or less, the occasional variation on a time-scale of 100 s means that the emission region is smaller than the radius, and is probably a few hotspots above the accretion disc. Relatively small radii ($\lesssim 20 r_g$) for the line-emitting region implied by the disc-line fit (Tanaka et al. 1995) suggest that the X-ray continuum source should be just above the disc surface, and orbits around the cental hole with the disc (Fabian et al. 1995).

4.2   Variability of the narrow- and broad-line components

We detect significant change not only in line flux but also in line profile (Figs 4, 5, 6 and 7). A clear result comes from spectral fits to time-ordered data. Characterizing the iron line as a narrow plus broad component, the intensity of the narrow component correlates with the continuum flux whereas the intensity of the broad component possibly anticorrelates. These line variations are evident in the two time intervals, the bright flare (*i*-3) and the deep minimum (*i*-7). As the EW of the narrow component can be a constant, the broad component is plausibly responsible for the line shape changes found in this study. This is consistent with the study of the light curves of the broad line/continuum bands and the narrow line/continuum bands (Section 3.4 and Fig. 11).

Since the light-crossing time of the line-emitting radius is shorter than each interval, we do not expect to detect any lag of the line. The correlated variability of the narrow-line component is then reasonable, although the behaviour of the broad component is difficult to understand.

However, results from the intensity-sorted data suggest that this behaviour of the line components is no longer valid, on taking shorter time-scales. The first attempt using the whole data set (Section 3.3.1) is largely affected by the extreme lines during the above two time intervals. Discarding the bright flare and the deep minimum, the intensity-sorted spectra provide clues to line variability accompanying continuum change on shorter time-scales of less than 10^4 s (Section 3.3.2). The correlation between the narrow component and the continuum disappears and there is a clear increase in the broad component during the high continuum flux data in which many brief flares are seen.
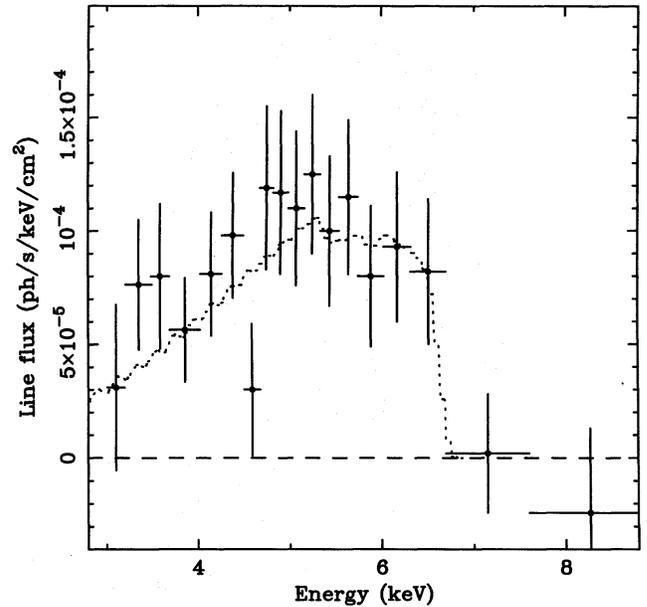
Figure 12. The line profile obtained from the deep minimum (*i*-7). Data from both S0 and S1 detectors have been summed. The profile has been corrected for absorption by the warm absorber and the detector response. The dotted line indicates a computed disc-line model for a Kerr metric (Laor 1991), assuming inner and outer radii of $R_{in} \sim 1.24 r_g$ and $R_{out} \sim 20 r_g$ of the disc inclined by $i = 30°$, and a radial emissivity index of $\alpha \sim 3$.

Summarizing the results of the line variability: (1) the narrow component follows the continuum if its variation is averaged over a few $\times 10^4$ s; (2) typical continuum changes on short time-scales (from 10^3 s to 10^4 s) appear to be followed by an immediate response of the broad component but not of the narrow component; and (3) the broad component changes in a different manner when the source changes its flux over long time-scales (a few $\times 10^4$ s) such as seen in the bright flare and the deep minimum, which makes the line profile unusual during those time intervals. Implications of this behaviour are discussed below.

4.3   Evidence for strong gravity around a Kerr hole

The huge red tail observed in the deep minimum suggests that the line should be produced at very small radii (e.g. 1.24–10r_g), requiring the Kerr geometry of a spinning black hole in which an accretion disc is dragged into inner radii closer to the black hole than in a Schwarzschild geometry. Since enormous gravitational effects are operating at such small radii, the line from the blue side is also gravitationally shifted into the red wing. As a result, almost all of the line emission goes to the broad red wing (Fig. 12).

The observed EW of this line (EW ~ 1 keV) is much larger than normally expected even if a reasonable overabundance of iron is taken into account (e.g. George & Fabian 1991; Reynolds, Fabian & Inoue 1995). Considerable amounts of radiation from very small radii of the disc can, however, be expected to return to the disc surface by light bending for a rapidly spinning black hole (returning radiation: Cunningham 1976). It is therefore possible that reflection will be enhanced by a factor of 2 (see table 5 in Cunningham 1976) so that a large equivalent width of the iron line is produced. Strong reflection is also consistent with the result of the warm absorber, reflection and broad-line fit (Fig. 8 and Table 4). Another possible reason is an ionized disc. A factor of ~2 larger EW for Fe xxv than

for cold iron could occur (Matt, Fabian & Ross 1991; Życki & Czerny 1992), combined with the returning radiation. A fit with the disc-line model from Laor (1991) for the line energy of 6.7 keV appropriate for Fe xxv gives a slightly better fit than in the case of 6.4 keV ($\Delta\chi^2 = 1.5$) with a steeper $\alpha = 3.4^{+0.6}_{-0.8}$ (see Table 3).

4.4 The line profile of the bright flare

On the other hand, the line shape is dominated by the narrow core around 6.4 keV during the bright flare (*i-3*). Here the narrow component follows the continuum whilst the broad component does not (Section 3.2.3). The unusually high narrow-core/red-wing ratio does not fit the disc-line model. A possible explanation for this is given here. The brightening of the continuum in this interval is of rather a longer time-scale (~30 ks) than the other many brief flares in which X-ray flux increases/decreases on time-scales typically less than 10 ks. Suppose that during this interval most of the activity is from a large flare at say $7r_g$ occurring above the blue (approaching) side of the disc. (A ring at this radius still has a large blue horn.) The line then comes mostly from the blue side of the disc where the blue peak dominates and the red wing of the line is depressed. As noted by Fabian et al. (1995), the effects of beaming from orbital motion of the disc on the line and continuum could help slightly here. The beaming factor for the photon rate varies as $\sim(1 + z)^3$ where z is the redshift, and is about ±30 per cent at a radius of $7r_g$ for a disc inclined by 30°. The expected slightly larger EW of the narrow component is compatible with the observed EW (Fig. 4). In this case, the duration of the bright flare (~30 ks) should be about half an orbit of the accretion disc or less, which implies $M_7 r_1^{3/2} \gtrsim 6$. Given a continuum flaring radius of $\sim 7r_g$ ($r_1 \sim 1$), the mass of the black hole is then about 6×10^7 M$_\odot$ or more. (If the mass is less than this, the narrow-core-dominated line shape could be due to a succession of flares on the approaching side of the disc.)

4.5 Line variability on long and short time-scales

The variability of both the broad and narrow components of the line is found to be separated into long and short time-scales (Section 4.2). This suggests that we are seeing different features of line production. In particular, the behaviours of the broad component in the bright flare and the deep minimum are remarkably distinct from the other time-intervals, as discussed above. The anticorrelation between the broad component and continuum seen in the time-ordered data might be a chance occurrence and requires confirmation by future observations.

The different line response depending on time-scale can be related to where the continuum and the line are produced. Rapid continuum changes such as those due to many distinct brief flares could occur mainly at small radii ($r < 6r_g$) where only a broad component is produced, so that the broad component follows the flares. The constancy of the narrow component on short time-scales may then be due to a constant background of emission from larger radii (say $6 - 10r_g$), which changes only on longer time-scales. (If instead the lack of instant response of the narrow line is due to the time lag effect, the black hole mass can be constrained as a function of r_1 and a typical time-scale of the continuum changes, e.g. if a typical time-scale of each brief flare is about $5000\tau_5$ s, then the light crossing time of the line-emitting radii, $500M_7 r_1$, is larger than that, giving $M_7 r_1 \gtrsim 10\tau_5$.) In this picture the bright flare is due to a flare or succession of flares on the blue side of the disc at $\sim 7.5r_g$, and the deep minimum is due to a simultaneous reduction in the background of emission from the outer regions ($r > 6r_g$) and increase of emission from the inner regions ($r < 6r_g$).

The net result on line variability is that the line is variable but complicated, and we have found no simpler single explanation other than a moving pattern of emission from a highly relativistic disc. Complicated line variability may result from multiple X-ray sources flaring at different radii on the disc, and involve orbital motion of the disc. A larger detector (or a much brighter source) is required in order to make firm progress.

4.6 Comparison with other observations

We note that a similar relationship between equivalent width of iron K line and continuum flux has been found in another broad skewed line object, IRAS 18325−5926 (Iwasawa et al. 1996). The EW is 500−800 eV during the *ASCA* observation, higher than the EW = 390 ± 150 eV during the *Ginga* observation (Iwasawa et al. 1995). The larger value of equivalent width of the *ASCA* data was obtained at an averaged flux level a factor of 3 lower than in the *Ginga* observation. It generally appears that a large EW tends to be observed when a source is faint (e.g., Iwasawa & Taniguchi 1993).

4.7 Contribution from a torus

We now comment on reflection from the putative molecular torus. Since the torus is thought to be outside the broad-line region, ~ 1 pc away from the central source, the torus emission basically remains constant at a certain averaged intensity level, whereas the reflection from the disc is supposed to follow the continuum source immediately. If there is a torus, when the source is faint such as in the deep minimum then the torus emission should be pronounced. Such a reflection spectrum is inevitably accompanied by a sharp 6.4-keV emission line (e.g. George & Fabian 1991), as observed in the *ASCA* spectrum of NGC 2992 (Weaver et al. 1996), and incompatible with the observed spectrum of the deep minimum. An upper limit of the narrow-line equivalent width is EW ≤ 196 eV, of which ~120 eV must be taken by the disc-line if the narrow core keeps a constant EW. Taking account that the average flux level is greater by a factor of ~2 than that in the deep minimum, any line from a torus imposed on the average continuum of MCG−6−30−15 has EW ≤ 40 eV. This value is much smaller than EW ≃ 600 eV as observed in NGC 2992 (Weaver et al. 1996), and implies that the reflection from the torus has little effect on the continuum of the deep minimum, and that its solid angle is small ($\Omega/2\pi \lesssim 1/4$), or the column density is less than $N_H \sim 10^{23}$ cm^{-2}.

5 CONCLUSIONS

The iron K line in MCG−6−30−15 shows significant variability in both intensity and profile when the continuum source changes. Selecting the two extreme time intervals corresponding to a bright flare and a deep minimum, we find a clear difference from the profile at other, intermediate, flux levels. At these two times the narrow core clearly correlates with the continuum flux whereas the broad wing possibly anticorrelates. In particular, the line profile of the deep minimum shows a huge red tail for which the Kerr metric is appropriate. These changes in line profile are understandable in terms of a relativistic accretion disc around a spinning black hole. In contrast, on short time-scales of less than 10^4 s, we find evidence that the broad wing increases as the continuum flares, whereas this

time the narrow core remains unchanged. This suggests that different regions produce the line at different times.

REFERENCES

Cunningham C., 1976, ApJ, 208, 534
Ebisawa K., 1991, PhD thesis, University of Tokyo, Tokyo, Japan
Fabian A.C., Rees M.J., Stella L., White N.E., 1989, MNRAS, 238, 729
Fabian A.C. et al., 1994, PASJ, 46, L59
Fabian A.C., Nandra K., Reynolds C.S., Brandt W.N., Otani C., Tanaka Y., Inoue H., Iwasawa K., 1995, MNRAS, 277, L11
Ferland G.L., 1991, Ohio State University, Astronomy Department Internal Report 91-01
George I.M., Fabian A.C., 1991, MNRAS, 249, 352
Kunieda H., 1995, in Appenzeller I., ed., Highlights of Astronomy, Vol. 10. Kluwer, Dordrecht, p. 513
Lightman A.P., White T.R., 1988, ApJ, 335, 57
Mushotzky R.F., Fabian A.C., Iwasawa K., Kunieda H., Matsuoka M., Nandra K., Tanaka Y., 1995, MNRAS, 272, L9
Iwasawa K., Taniguchi Y., 1993, ApJ, 413, L15
Iwasawa K., Kunieda H., Tawara Y., Awaki H., Koyama K., Murayama T., Taniguchi Y., 1995, AJ, 110, 551
Iwasawa K., Fabian A.C., Mushotzky R.F., Brandt W.N., Awaki H., Kunieda H., 1996, MNRAS, 279, 837
Laor A., 1991, ApJ, 376, 90
Matt G., Fabian A.C., Ross R.R., 1991, MNRAS, 262, 179
Nandra K., Pounds K.A., 1992, Nat, 359, 215
Nandra K., Pounds K.A., 1994, MNRAS, 268, 405
Nandra K., Pounds K.A., Stewart G.C., 1990, MNRAS, 242, 660
Otani C. et al., 1996, PASJ, 48, 211
Pounds K.A., Nandra K., Stewart G.C., George I.M., Fabian A.C., 1990, Nat, 344, 132
Reynolds C.S., Fabian A.C., Inoue H., 1995, MNRAS, 276, 1311
Reynolds C.S., Fabian A.C., Nandra K., Inoue H., Kunieda H., Iwasawa K., 1995, MNRAS, 277, 901
Ross R.R., Fabian A.C., 1993, MNRAS, 261, 74
Stella L., 1990, Nat, 344, 747
Tanaka Y., Inoue H., Holt S.S., 1994, PASJ, 46, L137
Tanaka Y. et al., 1995, Nat, 375, 659
Weaver K.A., Nousek J., Yaqoob T., Mushotzky R.F., Makino F., Otani C., 1996, ApJ, 458, 160
Yaqoob T., Warwick R.S., 1991, MNRAS, 248, 773
Yaqoob T., Edelson R., Weaver K.A., Warwick R.S., Mushotzky R.F., Serlemitsos P.J., Holt S.S., 1995, ApJ, 453, L81
Życki P.T., Czerny B., 1992, MNRAS, 266, 653